Check for updates

Intensified cross-linking dramatically improved the mechanical properties of hydroxyapatite and cellulose composites for repairing bone segmental defects†

Qingyou Liang, [ID]‡[ab] Jie Dong,‡[c] Jian Ren,[a] Cairong Xiao[a] and Chunlin Deng [ID]*[a]

Bone segmental defects (BSDs), common in bone injury, often occur in the long bones of limbs. Biomaterials are essential for bone repair, especially in cases of bone nonunion. The inorganic and organic phases in natural bone are tightly cross-linked, which provided the inspiration for the design of the composite materials for repairing BSDs. At present, natural ingredients are good candidates for such materials. However, their poor mechanical properties compared with natural long bones hindered their applications. Herein, it is crucial to understand the relationship between the intensified cross-linking inside the material and the improvement of mechanical properties. Therefore, we fabricated composite materials comprising hydroxyapatite (HA) and cellulose fibril (CF) with a water-mediated molding method. Cross-linking inside the material was intensified by applying high pressure and designing several cross-linking sites with covalent, ionic, and hydrogen bonds (H-bonds). The compression strength, modulus, and toughness were dramatically improved compared with those of existing comparable materials. For the first time, both the strength (137.2 MPa) and toughness (1.268 kJ m^{-2}) were within the ranges of human cortical bone, with a modulus of 1.6 GPa. Covalent and ionic bonds were strong and able to cross-link HA and CF tightly with phosphorylated sites. Besides, there were numerous sites for H-bonds, and water played an important role in H-bond formation. Ionic-wind-enhanced Raman spectroscopy (IWERS) was firstly utilized to analyze H-bonds of water itself without interference of other components. IWERS revealed the change of water H-bonds with different energies, which showed that water had enhanced H-bond interactions with other components. Intensified cross-linking was able to impart superior mechanical properties to the composite material. The *in vitro* and *in vivo* tests showed that the composite material had good biocompatibility and promoted the mobility of rats with tibia segmental defects. We anticipate that with further improvements in mechanical properties by means of intensified cross-linking mechanisms, this material can be applied in clinics.

Introduction

Bone is an important organ in the human body that protects the viscera and mechanically supports our bodies. Bone can be classified as cortical (compact) and spongy (trabecular) bone.[1] Long bone, a type of cortical bone that mainly exists in the extremities, has high strength, modulus, and toughness. Bone

segmental defects (BSDs) often occur because of injury, infection, and tumor.[2,3] When the defect length exceeds 5 cm (the critical size of bone defects), it is called a large bone defect that often leads to nonunion of the bone.[4] Therefore, a bone-repair material, which includes several types, is important for repairing BSDs.[5] Methods using natural bone include autologous bone grafting, bone allografting, the induced membrane technique (Masquelet technique), and distraction osteogenesis. However, problems such as limited sources from patients themselves, disease infection, or immune reactions hinder their applications. Therefore, artificial bone-repair materials are crucial for BSD repair,[6,7] with metals, ceramics, and polymers being most commonly used. Ideal bone-repair materials simultaneously meet the following requirements: osteogenesis, biosafety, low cost, and suitable mechanical properties; thus, the materials should have good bioadaptability.[8,9]

[a] *School of Materials Science and Engineering, South China University of Technology, Guangzhou 510640, China. E-mail: chldeng@163.com*

[b] *Analytical and Testing Center, South China University of Technology, Guangzhou 510640, China*

[c] *Department of Radiation Oncology, The Third Affiliated Hospital of Sun Yat-sen University, Guangzhou 510630, China*

† Electronic supplementary information (ESI) available. See DOI: https://doi.org/10.1039/d3ma00974b

‡ Qingyou Liang and Jie Dong contributed equally to this work.

As bone-repair materials, metals and ceramics have higher strength and modulus than the natural bone, resulting in a negative effect—stress shielding. Conversely, the toughness of polymers is often too high, resulting in different yielding behaviors from natural bones. Mechanical adaptability is a key issue with existing bone-repair materials because appropriate strength, modulus, and toughness are difficult to achieve simultaneously.[10] As the properties of a biomaterial highly rely on its components and structures, the natural bone inspires us in the design of bone-repair materials. Bone serves specific functions through complex and delicate structures. Human bone is composed of an inorganic phase (HA), an organic phase (collagen), and water. Mineralized collagen fibrils, which form oriented osteons as the basic unit of bone, comprise the fundamental structure of bone.[1] Although both HA and collagen are continuous, they are intertwined. These specific structures endow bone with excellent properties of high strength, modulus, and toughness. Composition and cross-linking at the nanoscale play a crucial role in the mechanical properties of bone.[1] Additionally, water is an important factor. Water molecules can form hydrogen bonds (H-bonds) with HA and collagen. H-bonds can appear and disappear dynamically, thus providing continuous interactions when bone undergoes stress. Therefore, cross-linking among component molecules is critical for strengthening and toughening BSD repair materials. Cross-linking is intensified by the formation of large numbers of chemical bonds, including covalent bonds, ionic bonds, and H-bonds.[11–15] The covalent and ionic bonds are strong bonds with energies >100 kJ mol^{-1}. Although the energy of H-bonds is often one order of magnitude lower than that of covalent and ionic bonds,[16,17] the number of H-bonds in natural bone is large. A high number of H-bonds is thus an important consideration in the design of the bone-repair material.[18–21]

Natural materials have attracted the attention of researchers owing to their higher bioactivity, better biocompatibility, and lower cost than artificial materials. And naturally-sourced composite materials have been fabricated, using both inorganic and organic components to benefit from their unique properties. However, current composite materials incorporating natural ingredients still have lower mechanical properties than long bone.[22–24] Therefore, effective design capable of intensifying cross-linking inside the material must be developed for mechanical adaptation (suitable compression strength, modulus, and toughness) in BSD repair. Hydroxyapatite (HA) is the main component of natural bones and is the most commonly used bone-repair material. HA has been composited with many natural polymers, including collagen, gelatin, cellulose, and chitosan. Cellulose is a natural polymer with multiple hydroxyl groups that act as cross-linking sites with other components. Besides, the crystalline region in cellulose has high modulus that aids in mechanical improvement.[25,26] Therefore, HA and cellulose were good candidates for the composite material for BSD repair.

Furthermore, this work employed a comprehensive preparation method to synthesize such composite materials with intensified cross-linking (Fig. 1a and b). Quantitative filter paper was used as the source of cellulose because it is cheap and contains pure and high-quality cellulose with trace residues (Fig. S1a and S2a, ESI†). The filter paper was hydrolyzed and treated with phosphoric acid to decrease fibril dimensions and add phosphate groups.[27,28] Then, calcium hydroxide $(Ca(OH)_2)$ was gradually added to the cellulose fibril (CF) suspension, and HA was generated in situ at a pH equal to 13–14 followed by the addition of additives for further cross-linking. Next, suction filtration was performed and the final material was molded at high pressure. HA and CF were cross-linked tightly in this process. Water was also introduced and able to mediate the molding process. At the same time, calcium ions (Ca^{2+}), hydroxyl groups/ions, and water molecules are capable of generating strong H-bonds, thus greatly improving the interactions among molecules. Compared with the current similar materials, this new composite material dramatically improved the three mechanical properties simultaneously.

The strengthening and toughening mechanisms were then analyzed using several instrumental methods. Especially in Raman analysis for H-bond of water, the water peak could not be fully observed using traditional methods, due to the fluorescence of the material and the detection range of the camera. Therefore, a novel method, ionic-wind-enhanced Raman spectroscopy (IWERS), was firstly utilized for the analysis of water H-bonds.[29] The IWERS method was totally nondestructive and noncontact, and able to minimize the influence of HA and CF on the water peak. In the end, in vitro tests were employed to verify the biocompatibility of the composite material and expression of related mRNAs of cytokines. Because tibial diaphysis defects are the most common problem in BSDs, a segmental tibia of Sprague–Dawley (SD) rats was replaced by this material in the experiment. The mobility of implanted rats was observed, and microcomputed tomography (micro-CT) and Masson stain were employed for morphological and histological analyses to assess the effectiveness of the material.

Experimental

Preparation of the composite material

Quantitative filter paper (1.5 g) with a diameter of 11 cm (Whatman brand) was pulverized for 3 min and then added to 75 mL of 75% (v/v) phosphoric acid. The solution was heated at 60 °C in a water bath for 5 h for esterification reaction. The obtained slurry was immersed in the solution for 3 days. Next, the suspension was centrifuged to remove the excess phosphoric acid. Then, the same volume of deionized water was added to the centrifuge tube to dilute the residual phosphoric acid, and the slurry was centrifuged again. The centrifuge process was repeated another 2–3 times. Thus, the CF was obtained and transferred to a 250-mL beaker. Pure phosphoric acid (0.1–1.1 mL 85% (v/v)) was added to the beaker to control the mineral phase content between 50 and 70%, followed by neutralization with a 1% (w/v) $Ca(OH)_2$ suspension. The reaction was performed under continuous stirring and the $Ca(OH)_2$ suspension was added dropwise until the pH reached 13–14. The suspension
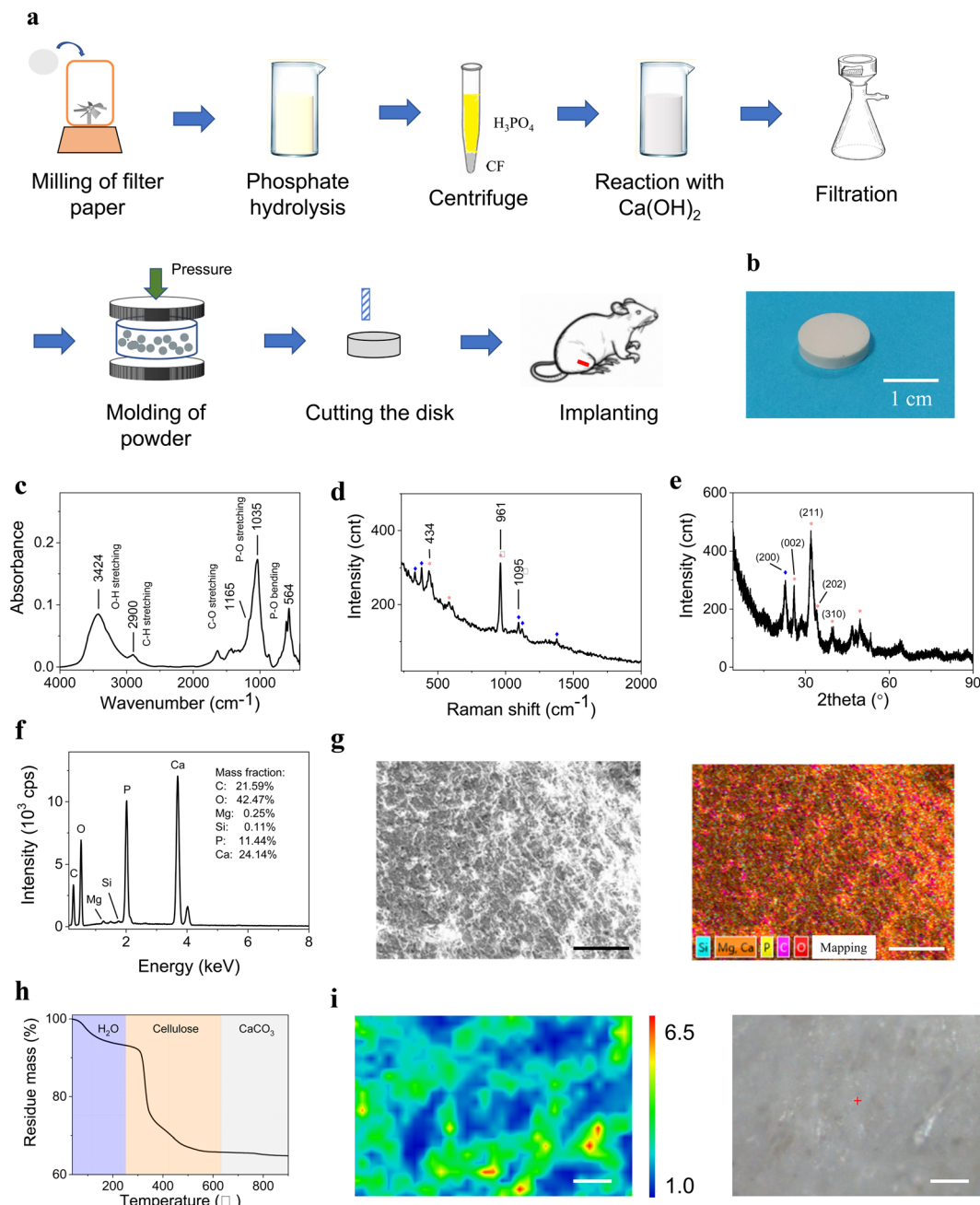
Fig. 1 The preparation process and characterization of the composite material. (a) The preparation process and photograph of the composite material. (b) Photograph of the disk of the composite material. (c)–(e) Spectroscopic characterization of the composite material using FT-IR (c), Raman (d), and WAXD (e). (f) Elemental analysis using EDS. (g) EDS mapping (scale bar: 250 μm). (h) TGA analysis for determination of the material components. (i) Raman mapping and optical photograph of the same area showing that HA grew in contact with CFs (scale bar: 100 μm).

was left overnight to react completely. Then, 34.4 mg of succinic acid, 8.6 mg of sebacic acid, 8.6 mg of dodecanedioic acid, 34.4 mg of $CaCl_2$, 34.4 mg of PEG4000, and 8.6 mg of glycerol were added to the as-prepared material. After stirring, the mixture was filtered by suction filtration to obtain the filter cake. The filter cake (0.7 g) was ground in an agate mortar and transferred to a 13-mm diameter stainless-steel mold, which was placed on the universal testing machine. The largest load of the machine was set to 70 kN (526 MPa). The pressure increased at the given rate while the mold

was maintained at the set temperature. The related parameters were optimized according to the experimental design. Finally, the composite material was obtained as a white disk with a diameter of 13 mm, which was cut using a screwdriver for subsequent testing. To investigate the influence of water, four samples were prepared. The "normal" sample was air-dried until there was no excess water on its surface. The "dry" sample was heated under an infrared lamp for 2 h (70–80 °C). The "wet" sample was sprayed with a moderate amount of water via a sprinkler, and sufficient

water was added to the "full" sample before it became a slurry. The pressing process was the same as above.

Characterization of mechanical properties

The compression strength and modulus were tested utilizing a universal testing machine. Considering that humans undergo a quasi-static impact in daily movement with a strain rate of 0.001–0.03 s^{-1} and there is only gentle movement under rehabilitation, a strain rate of 0.001 s^{-1} (0.06 min^{-1}) was used. The strength (unit: MPa) and the modulus (unit: GPa) were obtained from the stress–strain curves. The compression test is a type of static test. The toughness (impact strength) was determined by the falling ball method. The stainless-steel ball with a rod had a diameter of 5.98 mm and a total mass of 64.6650 g. The rod was constrained with a hole that was lubricated with silicon grease so that the ball was able to fall orthogonally and freely. The sample was placed under the ball and impacted by the ball until there was a crack on the sample surface or a tiny block fell off the sample. The height of the ball was recorded and the impact energy was calculated. The initial height of the ball was 1 cm and the ascending step was 0.2 cm.

Characterization of components

The material components were confirmed using several instrumental methods. Fourier transformation infrared (FT–IR) spectroscopy was utilized to obtain a component profile of the sample employing a Nicolet iS50 Fourier transform IR spectrometer with a wavenumber of 4000–400 cm^{-1} and a resolution of 4 cm^{-1}. The wide-angle X-ray diffraction (WAXD) spectrum was acquired using Cu Kα_1 radiation (λ = 1.5406 Å) with a generator current and voltage of 40 mA and 40 kV, respectively (X'pert Powder, PANalytical B. V.). The small-angle X-ray scattering (SAXS) data were obtained using a Xeuss 3.0 beamline with a minimum scattering angle of 0.82°. A laser confocal Raman spectrometer (DXR3xi, Thermo Scientific) provided the mapping results of a cross-section of the composite material with a wavenumber range of 100–2000 cm^{-1} and a resolution of 4 cm^{-1}. Thermogravimetric analysis (TGA) was performed using a TGA instrument (TG209F1, NETZSCH) under an air atmosphere at a heating rate of 20 °C min^{-1}. The temperature range was 40–900 °C so that CaCO$_3$ could decompose completely. The exact contents of the main components were determined using the TGA method. The morphologies of the samples were observed using scanning electron microscopy (SEM) (Merlin, Zeiss). The accelerating voltage was 5 kV and the working distance was 9–10 mm, which was beneficial for morphological observation of heat-sensitive samples. The energy dispersive spectrum was acquired using the same equipment for the elemental distribution information. High-resolution transmission electron microscopy (HRTEM) was employed to observe the combination of the inorganic and organic phases and crystal lattices and analyze the crystalline phase. The acceleration voltage was 200 kV (JEM-2100, JEOL).

IWERS conditions

IWERS is a powerful tool used to acquire Raman spectra under strong fluorescence and distinguish weak Raman peaks. In this work, IWERS was utilized for analyzing H-bonds of water in the composite material. The tip-net setup was utilized, which is a completely non-contamination and non-contact method. The voltage was −300 V, the curvature radius of the tip was 50 nm, the tip-net distance was 0.4 mm, and the net mesh was 40 mesh. The sample was placed ∼5 mm behind the net. IWERS was performed using a HJY LabRAM Aramis Raman spectrometer. The laser was selected as 633 nm and the power at the sample was 2 mW. The grating was 600 g mm^{-1} and the resolution was 4 cm^{-1}. Photobleaching was coupled with the ionic wind because they have a synergistic effect to quench fluorescence.

In vitro cytocompatibility test

The mBMSCs (Procell Life Science & Technology Co., Ltd, China) were selected to evaluate the cytocompatibility (cytotoxicity) of the material. The culture media was Dulbecco's Modified Eagle Medium with 10% fetal bovine serum and 1% penicillin/streptomycin (Gibco, USA). The mBMSCs were cultured in a 96-well plate with a density of 5 × 10^4 per well at 37 °C and 5% CO$_2$. The sample was extracted from the culture media (ISO 10993-12) and the extract was added to the mBMSCs. On days 1, 3, and 5 of incubation, the live–dead cells were stained and the number of cells was calculated. A calcein-AM/PI kit (Beyotime Biotechnology, China) was used to stain the cells and a Cell-Count-Kit 8 (CCK-8) (Dojindo, Japan) was used to determine the exact number of cells with a calibration curve produced with 450 nm. On day 7 of incubation, the culture medium was discarded. The plate was rinsed with phosphate-buffered saline twice. The cells were discomposed by adding 0.2% Triton X-100 (a surfactant). Then, the alkaline phosphatase (ALP) activity was determined using an ALP assay kit (Beyotime Biotechnology, China) and stained using a BCIP/NBT ALP color development kit. On the same day, RNA was extracted using an R1200 RNA extraction kit (Solarbio, China). The mRNA expression of the three cytokines, ALP, osteopontin (OPN), and Runt-related transcription factor-2 (RUNX-2), was amplified using real-time quantitative PCR (RT-qPCR) and determined using fluorescence. The $2^{-\Delta\Delta t}$ method was employed to calculate the expression level of these markers.

In vivo osseointegration test

Female SD rats were utilized to evaluate the supporting effectiveness and osteogenesis of the implanted composite material. The implanted group was defined as the rats that were removed with a segmental tibia (2.7 mm) and implanted with the material of the same size (n = 3), whereas the control group had only the defect of the tibia (n = 3). The defect of the tibia is one of the most common symptoms of bone defects; therefore, the tibia-defect model was used. The rats were anesthetized using an intraperitoneal injection of tribromethanol at a dose of 350 mg kg^{-1}. After depilation of the right hind leg, a material with a compatible diameter of the tibia was implanted. The material was fixed slightly using a thin thread that did not provide any support for the leg. The wound was closed carefully and penicillin was administered after surgery for 3 days. In the first 2 weeks, gypsum was used to fix the leg. From the third

week, the gypsum was removed and the rats could move freely. At the end of week 3, micro-CT was performed to observe osteogenesis *in vivo*. At week 4, the mobility of the rats was recorded and the MRT was calculated. After 5 weeks of implantation, the rats were sacrificed and the tibias were explanted for micro-CT and Masson stain examination. For micro-CT (SKYSCAN 1275, Bruker), the current was 75 μA, the voltage was 46 kV, the slice thickness was 20 μm, and the exposure time was 80 ms. For the Masson stain, the tibia was fixed using 4% paraformaldehyde first and was decalcified in an ethylenediaminetetraacetic acid (EDTA) solution for one month. A G1346 Masson stain kit (Solarbio, China) was applied for histological section and the collagen and osteocytes could be identified clearly. All the experiments were performed in compliance with the relevant laws and institutional guidelines, and were approved by the ethical committee at Yanxuan biological technology Inc. (approval number: HZYXSW2210193332).

Results and discussion

Material component characterization

The photos of the final product (Fig. 1b) show a round disk. The components of this composite material were analyzed using FT–IR, Raman spectroscopy, and WAXD. The representative spectra are discussed below. The FT-IR spectrum (Fig. 1c) confirmed that the components were HA and cellulose, where the 1035 cm^{-1} peak represents the stretching vibration mode of PO_4^{3-} (v_3) and the 565 and 602 cm^{-1} peaks represent the bending vibration mode of PO_4^{3-} (v_4). The 2900 cm^{-1} peak indicate cellulose. The peak at ∼3418 cm^{-1} represents the hydroxyl groups in CF and water.[30] For Raman testing (Fig. 1d), the 961 and 1095 cm^{-1} peaks were assigned to HA and CF, respectively. For the WAXD pattern (Fig. 1e), the peaks at 25.87°, 31.97°, and 39.47° represent the crystallographic planes of (002), (211), and (310) for HA, respectively. Using the peak at 25.87°, the crystallinity of HA was calculated as 83.37%. The peak at 22.69° represents the (200) plane of CF and the crystallinity of CF was 73.43% according to this peak (Fig. S7, ESI†). Some amorphous phases existed in HA and CF. All these techniques showed that HA and CF were the main components in the material and the HA content was higher than CF content, which was consistent with our design. Energy dispersive spectroscopy (EDS) in SEM (Fig. 1f and g) revealed that there was trace of magnesium (Mg) element in the material, which mainly came from the Ca(OH)$_2$ reagent and participated in HA formation (Fig. S2b, ESI†). Mg element was beneficial for osteogenesis. The content of every component was accurately determined using TGA (Fig. 1h). The TGA results were consistent with the data obtained *via* calculation of the original weights, which were recorded in the initial process. Therefore, the material contained the desired components with expected contents. Calcite (CaCO$_3$) was also present in the material at a much lower content than HA. Likewise, CaCO$_3$, which is also useful for osteogenesis, was not added to the sample directly and was generated by the reaction of Ca(OH)$_2$ and air along

with the formation of HA. The peaks at 1426 cm^{-1} in the FT-IR spectrum and 1086 cm^{-1} in the Raman spectrum confirmed this ingredient. The presence of CaCO$_3$ in natural bone suggests that the synthesis process was reasonable. Raman mapping of the cross-section of the disk showed that HA and CF were distributed uniformly. The CFs were entangled with each other and HA was in close contact with them (Fig. 1i and Fig. S2c, ESI†). Elemental distribution mapping using EDS revealed that all elements were distributed homogeneously, demonstrating that HA and CFs were cross-linked throughout the sample (Fig. 1g and Fig. S6, ESI†).

Mechanical properties under different conditions

The three mechanical parameters, compression strength, compression modulus, and toughness (also expressed as impact strength), were determined for each sample obtained under different conditions that influenced the different mechanical parameters. Strength reflects the ability to resist the largest stress (σ), whereas elastic modulus (E) reflects the extent of elastic deformation. These two parameters reveal the mechanical behavior under static load. Toughness (J) is the energy dissipated per unit area, which represents the behavior of the composite in the dynamic state. The natural bone bears the compression process in most cases. Therefore, the above three parameters are suitable for describing the mechanical behavior of the material.

All three parameters increased as the pressure increased at room temperature (25 °C) (Fig. 2a). From 10 kN (75 MPa) to 70 kN (526 MPa), the strength increased from 23.7 ± 1.5 MPa to 79.6 ± 12.1 MPa, the E increased from 0.45 ± 0.14 GPa to 0.88 ± 0.19 GPa, and the J increased from 0.710 ± 0.236 kJ m^{-2} to 1.144 ± 0.186 kJ m^{-2} ($p < 0.05$). Pressure (P) can dramatically improve the mechanical properties because it compacts the sample. Under high pressure, the molecules in the original material approached each other and began to coalesce. The spherical shape disappeared gradually and eventually coalesced completely. Small molecules and ions can also diffuse under high P, thus accelerating the coalescence.[15] The laser scattering analysis of the particle size distribution showed that following Ca(OH)$_2$ addition, the average particle diameter in the suspension was 92.0 μm (Fig. S5a, ESI†). The SEM image (Fig. 1g) showed a flat surface, indicating that the particles had coalesced. The apparent density of the representative sample was 1.9359 g cm^{-3} under 526 MPa, whereas the theoretical value was 1.9410 g cm^{-3}. Because the relative density was 99.74%, this preparation method could be regarded as a form of sintering.[15] The relative density of the 10 kN sample was only 74.86% and mechanical properties were very low. For example, the strength of the 10 kN sample was only 29.8% of that of the 70 kN sample. Therefore, we found that the P should be > 50 kN (376 MPa) during the preparation process.

Because there are two stages in the pressing process, the pressing speed was examined. The first stage was controlled by displacement and served as the prepressing stage. A low P of 5 kN (37.6 MPa) was achieved at the end of this stage. The second stage was controlled by force. Two speeds, 108 and
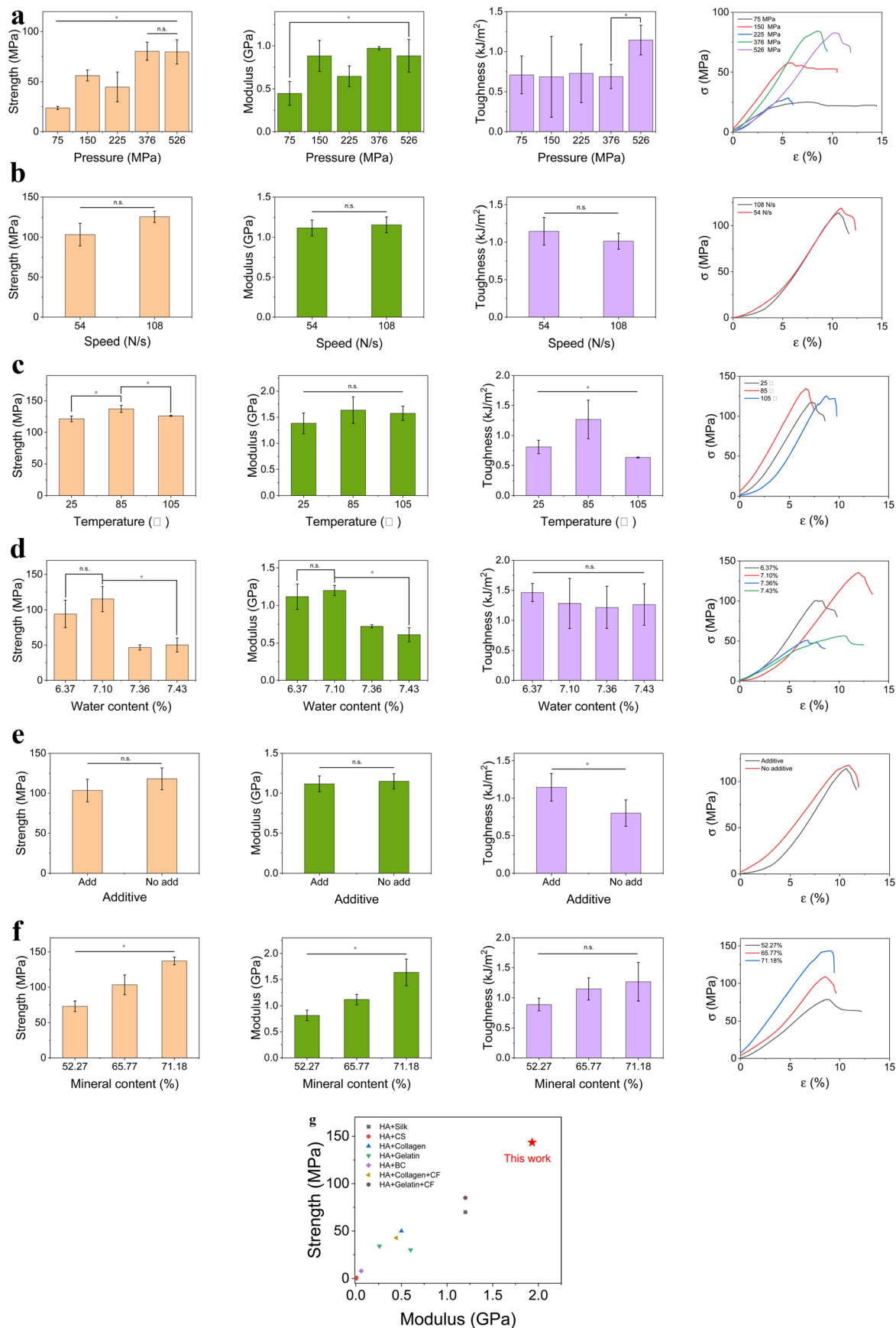
Fig. 2 The mechanical properties and force curve of compression under different conditions: (a) pressure, (b) compression speed, (c) temperature, (d) water content, (e) additives, and (f) mineral content. (g) Comparison of the mechanical properties of natural-source composite materials for repairing segmental bone defects in current references and this work. $*p < 0.05$; n.s. means no significance.

54 N s^{-1}, were tested and the strength under 54 N s^{-1} did not differ considerably from that under 108 N s^{-1} (Fig. 2b). Therefore, 108 N s^{-1} was selected. Next, the temperature (T) was optimized, which is an important factor for the final mechanical properties. The mechanical data (Fig. 2c) demonstrated that the strength and J at T of 85 °C were considerably higher than the results obtained at 25 °C and 105 °C. This indicates that although heating was important for molding, T that was too high was not beneficial. When T was increased from 25 °C to 85 °C, the mobility of water molecules increased and water dissipated more evenly in the material. Furthermore, water could act as a channel for ions and other molecules, allowing the particles to merge more effectively.[15] Higher T also provided more energy to the system for ingredient diffusion. However, 105 °C caused water to evaporate under relatively low pressure, which could result in a poorer distribution of water molecules and the destruction of the HA and CF crystal structures. Moreover, 105 °C approaches the starting decomposition temperature of cellulose.[31] Therefore, 85 °C was considered the best heating temperature. The phase diagram of water is noteworthy because water normally exists as a liquid at P of $\sim$0.5 GPa and $T > 25$ °C.[32] However, the nanoconfined water becomes ice (the configuration is flat rhombic) with a P of $\sim$0.5 GPa and a T of 25 °C.[33] If water molecules penetrate the CFs and form nanoconfined water, ice will develop at 25 °C and dramatically decrease the mobility and solvability of water, thus influencing the mechanical properties of the material.

The water content in the sample significantly influenced the mechanical properties (Fig. 2d). The mechanical properties of the samples with water contents of 6.37% (formerly named "dry"), 7.10% (formerly named "normal"), 7.36% (formerly named "wet"), and 7.43% (formerly named "full") were tested. Among the four samples, the sample with 7.10% water content had the highest strength and E values, which were significantly higher than those of the samples with water contents of 7.36% and 7.43% (nearly two folds, $p < 0.05$) but not significantly different from the sample with 6.37% water content ($p > 0.05$). All four samples had similar J values that were not significantly different ($p > 0.05$). This showed that different factors influenced the different parameters. Notably, it seemed unlikely that the negligible variations in the water content could render such large differences in mechanical properties. The water contents of the powders before molding varied considerably (see Methods) and the water in the disk only represented its final state. The excess water was lost during the pressing process. An appropriate amount of water can help the coalescence of particles, but too much water separates the particles and prevents them from interacting. Water is a crucial factor in the formation of H-bonds, which will be discussed in the next section.

Additives were also applied to the composite and J improved significantly from 0.801 ± 0.176 kJ m^{-2} to 1.146 ± 0.185 kJ m^{-2} ($p < 0.05$) (Fig. 2e). Dibasic acids (including succinic acid, sebacic acid and dodecanedioic acid) were expected to help covalent cross-linking through the ester structure. Polyethylene glycol 4000 (PEG4000) and glycerol have many hydroxyl groups capable of forming H-bonds. Furthermore, PEG4000

and glycerol dissolve Ca^{2+} ions and thus aid in ionic cross-linking.

The mineral phase in the composite is also crucial for mechanical behavior. HA is the main mineral phase and the main component in the material. A minor content of CaCO$_3$ was also present. The mineral phase content significantly increased the strength and E of the three samples with mineral phase contents of 71.18%, 65.77%, and 52.27%, respectively. However, J was not significantly influenced by the mineral content (Fig. 2f). The sample with a mineral phase content of 71.18% simultaneously produced the highest average compression strength, E, and J of 137.2 ± 5.5 MPa, 1.6 ± 0.3 GPa, and 1.268 ± 0.321 kJ m^{-2}, respectively, with the highest values of 143.5 MPa, 1.9 GPa, and 1.632 kJ m^{-2}, respectively. For human cortical bone, the ranges of strength, E, and J are 130–250 MPa, 4–30 GPa, and 0.6–3.0 kJ m^{-2}, respectively.[5] For the first time, both the strength and J values of the composite material were within the ranges of cortical bone. Although the E only reached $\sim$2 GPa, all parameters of our material were much higher than those of the current comparable materials (Fig. 2g). Furthermore, the disk with a mineral phase content of 71.18% had a relative density of only 94.28% (the apparent density was 1.9595 g cm^{-3}). Therefore, there is still space for improving the mechanical properties, such as increasing the P to 1 GPa or higher.[15]

Intensified cross-linking mechanisms that contribute to mechanical properties

Intensified cross-linking mechanisms on the molecular scale. Cross-linking enhances the connection and interaction of different units and molecules inside the material (Fig. 3a). Applying high pressure and designing several cross-linking sites are two crucial approaches to intensify cross-linking.[19] High pressure causes the material granules to come into close contact with each other, reducing the volume of the void. Therefore, the structural units of the final product will not bend under applied pressure.[34] Conversely, numerous cross-linking sites further tightened these structural units.

From the physical perspective, entanglement causes CFs to form an interlocking structure through cross-linking sites (Fig. S2c, ESI†). It will cost a great deal of energy to break the covalent chains of cellulose. Because the CF length was much longer than 100 μm in most cases, there were many opportunities for entanglement. The distribution of carbon (C) element can be regarded as the distribution of CFs because the C mainly comes from cellulose. The EDS image (Fig. 1h) indicates that the fibers curled up in three dimensions because most C element strips were <100 μm. Additionally, the fibers may extend from one granule to another, thus tightening neighboring granules.

From the chemical perspective, there are four types of interactions: covalent bonding, ionic bonding, van der Waals forces, and hydrogen bonding. H-bonds are a type of van der Waals interaction, although H-bonds are much stronger than the latter. Different cross-linking sites may have different interactions. First, covalent and ionic bonds were introduced
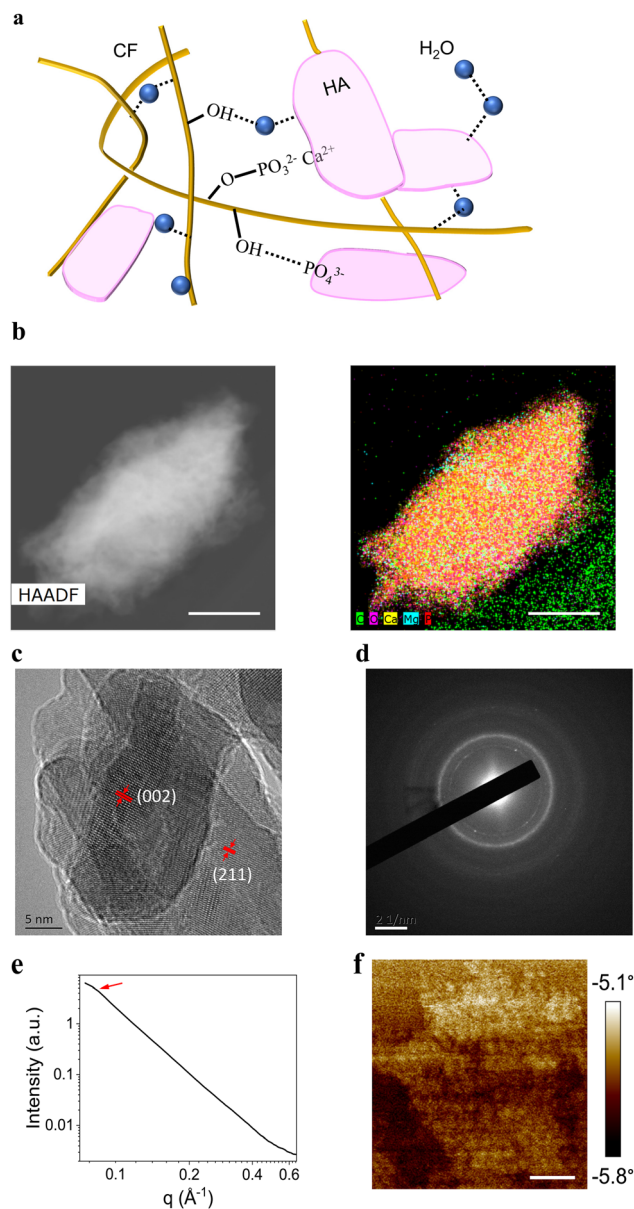
Fig. 3 The combination of HA and CFs on the microscopic scale. (a) Schematic diagram of the component interactions *via* different bonds. Solid line: covalent bond; dotted line: H-bond. (b) TEM image *via* HAADF and EDS mapping of the same area. (c) The HRTEM crystal lattice image confirming HA. (d) The TEM selected-area electron diffraction pattern. (e) The SAXS spectroscopy. (f) EFM image for HA deposited on a CF segment. The scale bars in figure b, c, d, and f are 200 nm, 5 nm, 2 nm^{-1}, and 1 µm, respectively.

low. However, the typical CF diameter was 10–20 µm and phosphoric acid was unable to penetrate deep into the fiber. Assuming that all three hydroxyl groups (–OH) on an individual saccharide ring were modified with phosphate groups, the calculation showed that the average penetration depth was 23 nm. EDS mapping using HRTEM showed a similar result: the mineral phase had penetrated the fiber to a depth of ∼20–30 nm according to the element distribution (Fig. 3b). Therefore, the cross-linking of HA and CF *via* covalent and ionic bonds was confirmed.

In natural bone, HA also penetrates the gelatin fiber and exists in the noncrystalline state, which suggests that the amorphous HA in this composite material may come from the HA inside CFs. The crystallization of minerals inside a fiber will induce large stress in the composite interface, thus strengthening the whole material.[35] In addition, the interwoven lattices will effectively increase the toughness of the material if the lattices are interpenetrating.[36] HRTEM further showed the crystalline grain (Fig. 3c). The black area in the center was the crystalline plane of (002) and the gray area was the (211) plane, which was the major peak of HA in WAXD. A grain size of ∼10 nm was obtained using the Scherrer equation for the WAXD pattern (Fig. 1f and Fig. S7, ESI†), which was similar to the HRTEM photograph. The diffraction rings of the selected-area electron diffraction revealed that the selected area was polycrystalline and the rings were assigned to the crystalline planes of (211), (002), and (310), which were consistent with the WAXD pattern of HA (Fig. 1f and 3d). The rings were diffusive in the area of the large scattering vector, demonstrating that HA was not completely crystalline. SAXS showed a weak peak at 0.0733 Å and the corresponding periodical length was ∼8.7 nm (Fig. 3e), which might be the distance of the small fibers on the surface of the main fiber. This might influence the size of HA crystals on the CF surfaces.

To further investigate the charge distribution on the mineralized fiber, electrostatic force microscopy (EFM) was employed (Fig. 3f). The mineral phase was deposited on the CFs on the micrometer scale. Although the quantity of charge did not vary much along toward fiber axis, it distinctly changed in the direction of the fiber radius. This demonstrated that a charge gradient existed at the interface between the mineral and fiber, thus intensifying cross-linking *via* ionic bonding. Infrared microscopy (IRM) was utilized to investigate the combination of the mineral phase and fiber on a millimeter scale (Fig. S8, ESI†). The mineral phase tended to grow along with the CFs. IRM and EFM demonstrated the suitable combination of the two phases both on the macroscopic and microscopic scales. As for additives, PEG4000 and glycerol were able to aid Ca^{2+} migration, thus also promoting cross-linking *via* ionic bonding.

Hydrogen bonding was another crucial factor to intensify cross-linking for dramatic improvement of mechanical properties. Although H-bonds are much weaker than covalent and ionic bonds, the material included more H-bonds than the other two bonds because H-bonds had more interaction sites. Thus, H-bonds could provide a considerable amount of energy to resist an external force. There were numerous sites for

into the system. Because the filter paper was hydrolyzed by H$_3$PO$_4$, the CFs were modified with phosphate groups (zeta potential of −11.8 mV, Fig. S5b, ESI†) that were able to react with Ca(OH)$_2$. Therefore, the covalent bonds of P–O and the ionic bonds between Ca^{2+} and the phosphate group were formed simultaneously. Both bond types were strong, and HA and CF were connected tightly. Titration measurement using Ca(OH)$_2$ revealed that the molar ratio of the modifying phosphate groups to the total CFs was 1.56 : 100. This data seemed

H-bond cross-linking, *e.g.*, –OH on the CF surface and OH$^-$ and PO$_4^{3-}$ in the HA crystal lattice.[37,38] Water played a key role in H-bond formation. FT-IR and Raman are both effective methods to investigate hydrogen bonding. The energy of the H-bonds can be calculated using FT-IR and the spectroscopic dissociation energy (D_e) can be expressed using the Morse function as follows:[39]

$$D_e^{mol} = \left(\frac{\tilde{\omega}}{1000}\right)^2 \times 42.0610 \quad (kJ\ mol^{-1})$$

where $\tilde{\omega}$ is the wavenumber (cm^{-1}) obtained from the FT-IR spectrum. The H-bond energy ($E_{H\text{-bond}}$) is thus equal to $D_{e,0} - D_{e,1}$, where $D_{e,0}$ is the original dissociation energy and $D_{e,1}$ is the shifted dissociation energy. The $\Delta E_{H\text{-bond}}$ values (the change of the H-bond energy) for CF, H$_2$O, and HA of the four samples with different water contents are presented in Fig. 4a. The sample with a water content of 7.10% showed the greatest positive $\Delta E_{H\text{-bond}}$ for CF and HA. The $\Delta E_{H\text{-bond}}$ of HA in this sample was a relatively large positive value, whereas it was slightly negative in the other three samples. The $\Delta E_{H\text{-bond}}$ of H$_2$O showed small variances among the four samples. These results demonstrated that the

H-bonds had a substantial effect on the mechanical properties of the composite. However, the O–H peak in the FT-IR spectrum was strong, and CF, H$_2$O, and HA all contributed to this peak. Owing to this interference, FT-IR could not be used to investigate the energy change of water itself. Nevertheless, the Raman peak intensity decreases when the fluorescence increases. A "moderate" fluorescence may reduce the influence of –OH of the CFs on water. Therefore, we developed IWERS with a 633-nm laser as a non-destructive technique to study these samples (Fig. 4b and Fig. S9, ESI†).[29] The H-bond strength is indicated by the wavenumber shift, in which wavenumbers >3410 cm^{-1} or <3310 cm^{-1} are regarded as weak or strong H-bonds, respectively, and wavenumbers in the range of 3410–3310 cm^{-1} indicate intermediate H-bond strength.[40] The IWERS results of water showed that the energy of strong H-bonds decreased and that of intermediate H-bonds increased compared with pure water. The number of intermediate H-bonds did not change, whereas the number of weak H-bonds increased and that of strong H-bonds decreased. This demonstrated that the H-bonds within water molecules were broken and new H-bonds were created between water and other components, in which the total energy of the intermediate H-bonds increased.
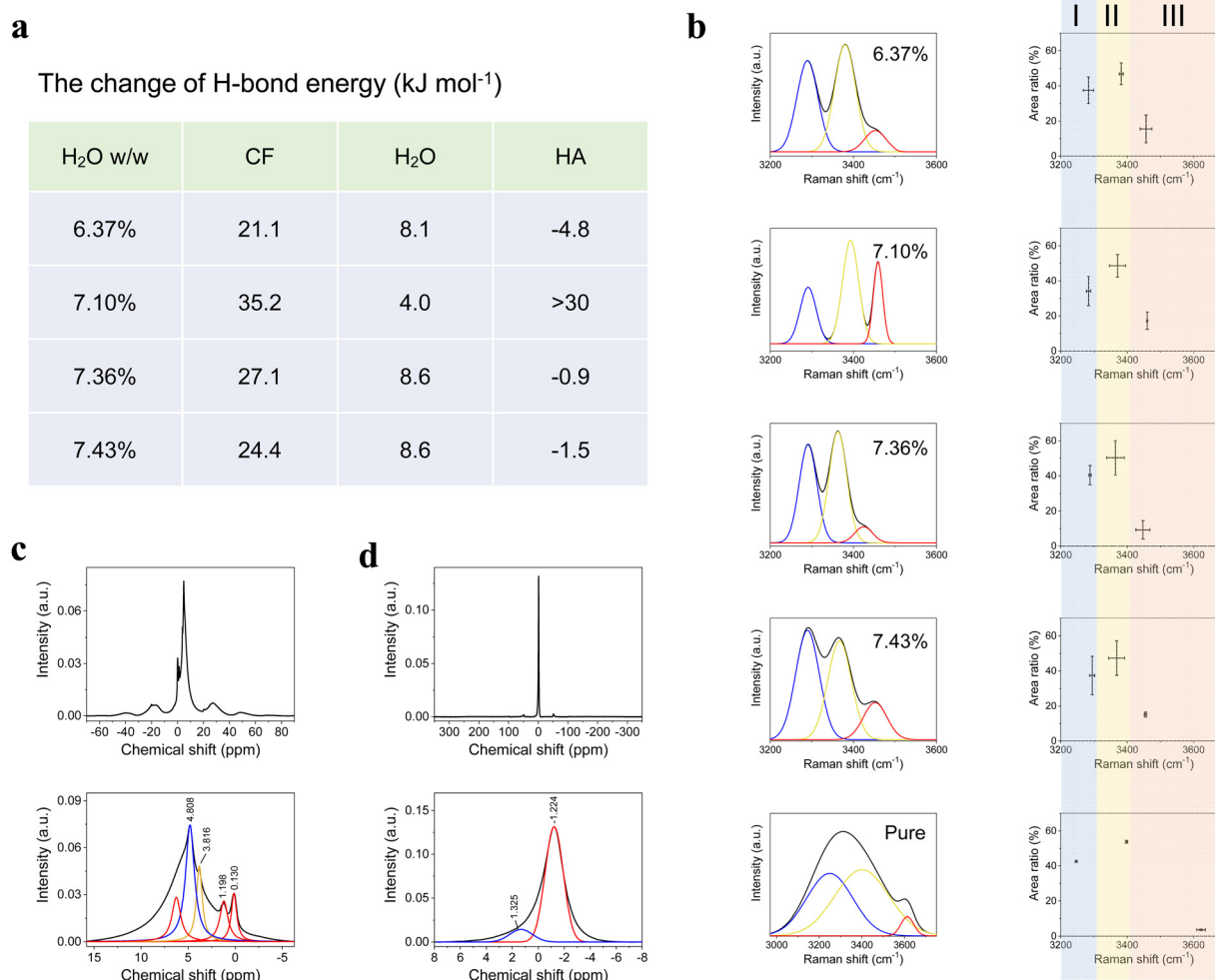

Fig. 4 The characterization of H-bonds. (a) The changes of the H-bond energy (DEH–bond) calculated from the FT-IR spectra. (b) IWERS analysis for the change in H-bond energy of water in the composite material. (c) ^{1}H-ssNMR spectroscopy and peak fitting. (d) ^{31}P-ssNMR spectroscopy and peak fitting.

The change of H-bond energy (kJ mol^{-1})

H$_2$O w/w	CF	H$_2$O	HA
6.37%	21.1	8.1	-4.8
7.10%	35.2	4.0	>30
7.36%	27.1	8.6	-0.9
7.43%	24.4	8.6	-1.5

Generally, the H-bonds among water molecules are unable to contribute to the mechanical properties of the material. However, after breaking, the H-bond sites of water molecules were released and the water was able to interact with the other components, thus intensifying cross-linking.

Solid-state nuclear magnetic resonance (ssNMR) spectroscopy was also employed to monitor H-bonds. The ^{1}H-ssNMR spectrum presented several peaks (Fig. 4c). The major peak at a chemical shift (δ) equal to 4.808 ppm was assigned to water. After the hydrogen exchange, –OH in the CF showed the same broad peak at this position. The peak of pure water was located at 4.6–4.7 ppm, which revealed that H-bonds were formed by these components. The peak at δ of 3.816 ppm was assigned to CH groups in CF. The two peaks at δ of 0.130 and 1.198 ppm were assigned to OH$^-$ in HA, where the latter peak could be indicative of H-bond formation.[41] There was only a single peak in the ^{31}P-ssNMR spectrum (Fig. 4d) at δ of -1.224 ppm. The upfield shift of the phosphorus resonance by 4–5 ppm revealed that H-bonds were generated between the oxygen atoms in PO$_4^{3-}$ and other components. ^{1}H-ssNMR and ^{31}P-ssNMR both indicated the presence of H-bonds. Under an external load, the H-bonds and ionic bonds were dynamic, allowing energy to be effectively dissipated.[42]

Intensified cross-linking mechanisms on the macroscopic scale. The previous section provided the strengthening and toughening mechanisms on the molecular scale, while SEM showed these mechanisms on the micrometer scale. When force was applied to the material, the slip line moved (Fig. 5a). The CF bent the slip line, which became longer. The slip plane thus cost more energy, indicating that the ability to resist the external force was enhanced and the composite was strengthened. The SEM image (Fig. 5b) shows the transversal cross-section of a compressed sample in which a long crack caused by the slip line was bent with a flexural degree of $>90°$ by a perpendicular thick fiber. The SEM image in Fig. 5c shows the longitudinal cross-section of the compressed sample. A crack appeared along one of the fibers, which was also caused by the slip plane. Both of the images showed an increase in consumed energy when the material was under load. There were several mechanisms for toughening. Fig. 5d shows the propagation of a twisted crack that stopped at the CF. Although the CF was torn off, the crack also ended. Breaking the CF consumed much energy from the crack so it was unable to propagate continuously. This mechanism was similar to the pinning process, in which a crack turns around an object like a nail and then stops.[43] Additionally, the direction of this crack was deflected 10 times across the linear distance of 10 μm, and the entire path length increased to 14 μm. Therefore, an additional 40% of the energy was dissipated. The longer crack (40 μm) in Fig. 5e made a large turn of $\sim90°$ overall, preventing straight propagation of the crack. This crack also diverged as it progressed. In the neighboring crack, a CF linked the two sides of the crack, which was just a bridging mechanism. Fig. 5f shows another bridging mechanism, in which a curled fiber unfolded and stretched out to form a flat "bridge" across the crack.[44] At this time, the "bridge" did not form inside the crack but on its surface. Fig. 5e also shows several tiny cracks. All of these mechanisms increased the toughness of the composite material.[45,46]

Biocompatibility and bioactivity tests *in vitro*. Biocompatibility was the important consideration of this implanted biomaterial, which was investigated using mouse bone marrow mesenchymal stem cells (mBMSCs). The number of live cells was determined using Cell Counting Kit-8 (CCK-8) and the
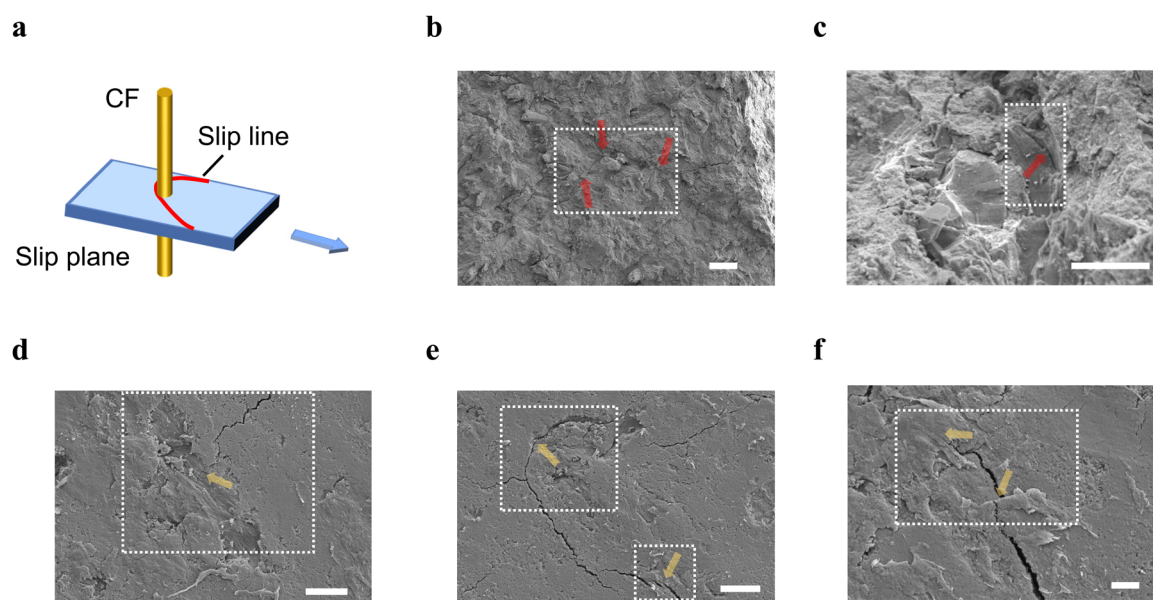

Fig. 5 The SEM characterization of the strengthening (a)–(c) and toughening (d)–(f) mechanisms. (a) Schematic diagram for strengthening. (b) The slip line on the transversal cross-section. (c) The slip line on the longitudinal cross-section. (d) The small turns and pinning of a crack that was stopped by CF. (e) A large turn and divergence of a crack, with a CF bridge inside the crack. (f) The bridges constituted by uncurled CF on the surface of a crack. The scale bars in (b)–(f) are 50, 10, 5, 5, and 1 μm, respectively.

optical density values were obtained under a 450-nm wavelength. The apoptosis ratio was defined as 1-cell viability (%). Fig. 6a shows that the ratio of the dead cells to all the cells was < 3% until day 5 for both the control and sample groups, between which there was no significant difference. Cell staining revealed that the cell morphology was normal for the two groups. Therefore, the composite material had no cytotoxicity.

ALP exists broadly in the liver, bone, and intestine.[47] In the early stage of bone repair, much ALP is expressed, which helps bone healing. ALP staining showed that the sample group had more ALP than the control group (Fig. 6b). The determination of ALP showed a significant quantitative difference between the two groups. The results are expressed in the ALP units of total proteins. The expression of mRNA of three cytokine proteins, ALP, OPN, and RUNX-2, was examined using the polymerase chain reaction (PCR) method. These cytokines play an important role in the process of ossification *via* complex cell signaling pathways.[48,49] OPN regulates osteoclasts, whereas RUNX-2, a transcription factor, regulates the expression of several genes, including OPN. On day 7 of the culture, the expressions of ALP, OPN, and RUNX-2 mRNA in the sample group were significantly higher than in the control group ($p < 0.001$) by 2.67-fold, 7.84-fold, and 6.60-fold, respectively (Fig. 6c). The increase in ALP gene expression revealed that mBMSCs were induced and

differentiated more effectively. The expression of OPN mRNA was higher than that of the other two genes. The main component of this material was HA, which needed to be degraded before the formation of new bone. Osteoclasts involve the process of mineral absorption.[50] Although there was no internal porous architecture in the implanted material, prior degradation of HA and minor cracks that formed *in vivo* may have provided sufficient space for osteoblasts.[51] *In vivo* experiments will be discussed in the next section.

The bioactivity test was also performed using a simulated body fluid (SBF) and a fast mineralization solution (FCS), respectively (Fig. S15, ESI†). After 3 days, several HA particles emerged on the sample surface for SBF, while numerous HA flakes generated for FCS. The results demonstrated that the material had good bioactivity.

Verification of mechanical properties *in vivo*. Because the composite material had good biocompatibility and bioactivity, the effectiveness of implantation was observed using *in vivo* tests, with examination of three groups (implanted, control, and normal) of SD rats. A segmental tibia (2.7 mm) was replaced by the composite material for the implanted group and the bone defect was left untreated for the control group. The moving response time (MRT) is the time taken from the beginning of the elevation of the implanted leg to the moment of touching the ground. The MRT reveals the agility and strength of the limbs and serves as an index of healthiness. As shown in Fig. 7a (week 4), the MRTs of the implanted and normal groups were 0.244 ± 0.080 s and 0.261 ± 0.037 s, respectively. There was no significant difference between the groups. Nevertheless, the MRT of the control group was 0.402 ± 0.040 s, which was significantly higher than that of the implanted group ($p < 0.01$). The results demonstrate that the mobility of the implanted group was much better than that of the control group and was similar to the MRT of the normal group. Therefore, the material implantation significantly improved the mechanical properties of the long bone. The gypsum plaster was removed only half a month after surgery, which is a relatively short time for common fixation. It can be speculated that patients with bone defects would benefit from this composite material due to earlier mobility and lower burden if this medical device were applied.

Micro-CT was utilized to observe osteogenesis *in vivo* (Fig. 7b for week 3) and *ex vivo* (Fig. 7c and d for week 5). The micro-CT photograph at the cross-section of the implanted material (right side) shows that the cortical bone formed a complete circle around the spongy bone. Compared with the normal leg (left side), the implanted region had a larger diameter, demonstrating that the bone still needed to be remodeled. The whole tibia was removed after the sacrifice of the rats and was examined using micro-CT and Masson stain. Micro-CT showed that the ratio of bone volume to tissue volume was 45.7% ± 6.8% and 51.3% ± 7.6% for the implanted and control groups, respectively, which were not significantly different and demonstrated that the bone quantity was the same. However, the control group exhibited disconnection of the trabecular bone of the tibia,[52] whereas the implanted group did not. The tibia in
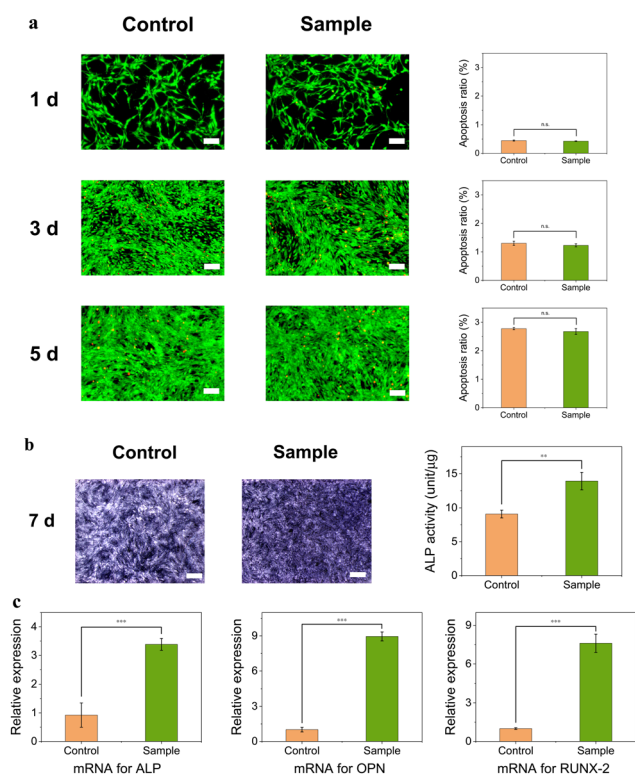

Fig. 6 Biocompatibility and expression of related protein and mRNAs *in vitro*. (a) Biocompatibility test for 5 days of incubation employing mBMSCs, which showed no cytotoxicity (scale bars in a are all 100 μm). (b) The relative ALP activity on the 7th day of incubation with the optical images (scale bars in b are both 500 μm). (c) The expression of mRNAs for the cytokines of ALP, OPN, and RUNX-2. **$p < 0.01$; *** $p < 0.001$; n.s. means no significance.
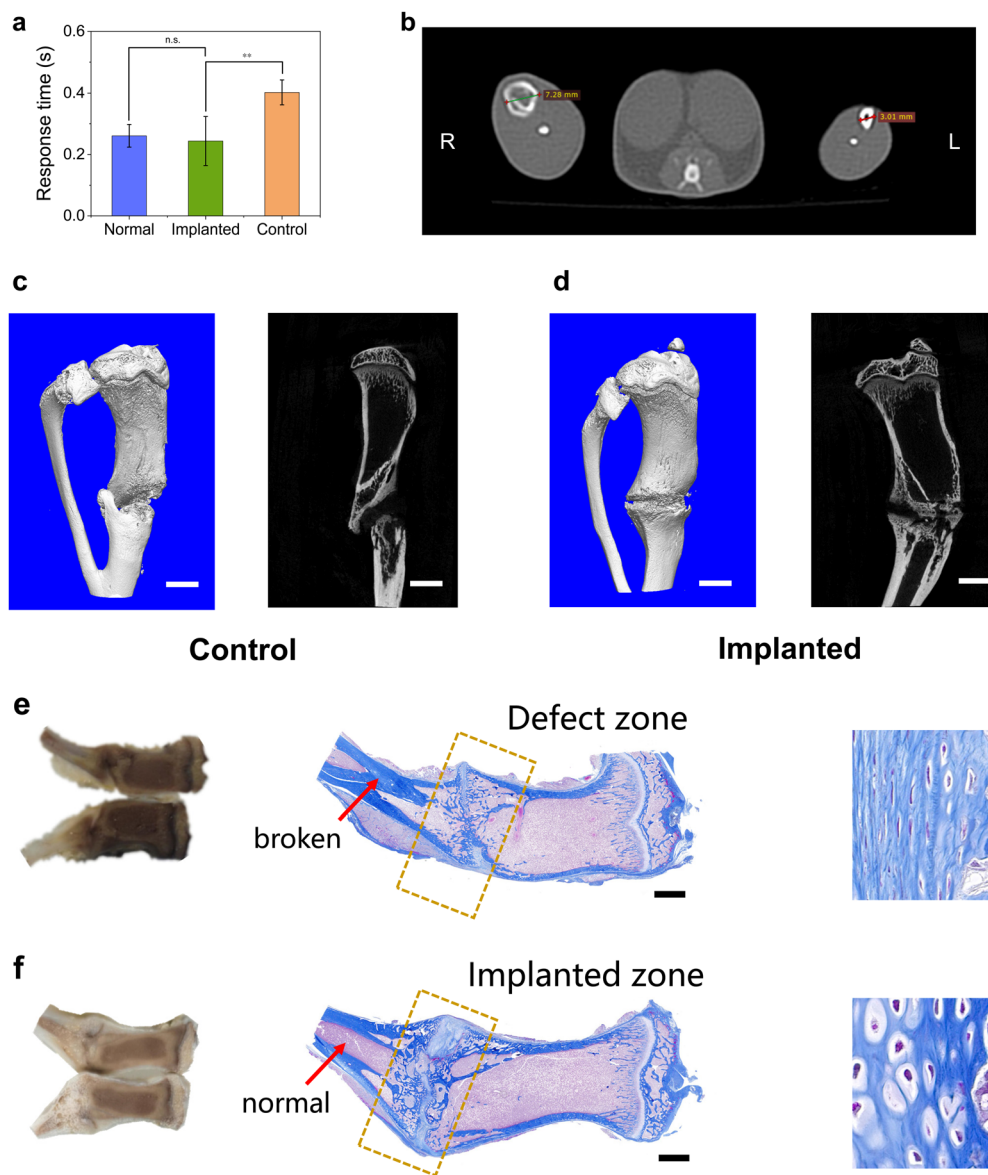
Fig. 7 Verification of implanting effectiveness *in vivo*. (a) The comparison of moving response time (MRT) for the normal, implanted, and control groups. (b) The micro-CT photograph of the tibia of the live rat at the 3rd week of implantation. (c) and (d) The micro-CT photograph of the tibia *ex vivo* for the control (c) and implanted (d) groups at the 5th week (scale bar: 3 mm). (e) The photograph and Masson stain image of the control group (scale bars are 2 mm and 20 μm for the middle and right images, respectively). (f) The photograph and Masson stain image of the implanted group (scale bars are 2 mm and 20 μm for the middle and right images, respectively).

the control group may have been overloaded and showed ectopic osteogenesis to some extent. In contrast, the implanted material dispersed the stress effectively and protected the tibia. In the Masson stain image (Fig. 7e for the control group and Fig. 7f for the implanted group), the cortical bone of the control group had obvious cracks and interrupted the trabecular bone, whereas the implanted group maintained a good morphology. This phenomenon showed that the implanted material homogenized the external load and matched the long bone with it, which was consistent with the micro-CT results. There was a light-white stripe across the defect region both in the implanted and control groups, indicating that new bone was forming and the healing was not completed yet. The arrows

indicate the nonexcision region. For the control group, the cortical bone had "invaded" the trabecular bone and broken it, whereas the implanted group remained normal. These results were consistent with the micro-CT results. In the zoomed images of the Masson stain, most of the bone cells in the control group were osteoblasts, whereas some of the osteoblasts had become osteocytes in the implanted group. Hematoxylin and eosin (HE) stain also gave similar results to Masson stain (Fig. S11, ESI†). This demonstrates that the implanted material may be of assistance to bone cell transformation. Although the composite material had low porosity, cracks would form when the material was soaked in water or implanted *in vivo*, thus providing enough space for cell growth (Fig. S12–14, ESI†).

Conclusions

Simultaneously achieving multiple properties including strength, modulus, and toughness has proven challenging in the development of artificial bone-repair materials.[53] The dedicated design of a composite material structure to intensify cross-linking is crucial for achieving this goal.[54,55] Naturally-sourced HA and CF were used in the composite material, which exhibited good biocompatibility, bioactivity, and mechanical properties for repairing BSDs. Hydrolyzing filter paper with phosphoric acid provided CFs with active sites that were able to react with $Ca(OH)_2$ to form a hybrid material. The water-mediated molding method with high pressure was applied to fabricate the composite, and different molding parameters had different influences on strength, E, and J. HA and CFs were heavily cross-linked by covalent, ionic, and H-bonds. HA and CFs penetrated each other via phosphorylated hydroxyl groups that formed ionic and covalent bonds. Strong H-bonds can form among HA, CFs, and water. Although H-bonds are much weaker than covalent and ionic bonds, the large number of H-bonds was able to provide strong cross-linking among molecules/ions. Water, which was distributed widely inside the material and formed large amounts of H-bonds with the other components, played a crucial role in cross-linking. The IWERS method confirmed that water molecules formed new H-bonds with other components, as the energy and number of strong, intermediate and weak H-bonds of water all changed. Apart from the cross-linking mechanisms on the molecular scale for dramatic improvement of mechanical properties, several strengthening and toughening mechanisms existed simultaneously on the macroscopic scale. The strength and J of this composite material were comparable to those of cortical bone, whereas there was still a gap for E. However, this work produced the highest values of the three mechanical properties for naturally-sourced materials. This composite had no cytotoxicity and could facilitate mobility and bone cell transformation of SD rats with tibia defects. Furthermore, it provided good mechanical support for the rats, enabling the MRT to recover to its normal state. The mechanical properties of the composite material can be further improved by means of intensified cross-linking mechanisms. Because this material is biomimetic and of low cost, it has great potential for actual applications.[6]

Author contributions

Qingyou Liang: writing – original draft, writing – review and editing, conceptualization, methodology, investigation, and validation. Jie Dong: methodology, investigation, and validation. Jian Ren and Cairong Xiao: methodology. Chunlin Deng: writing – original draft, writing – review & editing, conceptualization, supervision, and project administration.

Conflicts of interest

There are no conflicts to declare.

Acknowledgements

References

1 G. J. Tortora, *Principles of human anatomy*, Wiley, New Jersey, USA, 2002.

2 K. Zhang, Y. Zhou, C. Xiao, W. L. Zhao, H. F. Wu, J. Q. Tang, Z. T. Li, S. Yu, X. F. Li, L. Min, Z. T. Yu, G. Wang, L. Wang, K. Zhang, X. Yang, X. D. Zhu, C. Q. Tu and X. D. Zhang, *Sci. Adv.*, 2019, **5**, eaax6946.

3 C. Mauffrey, B. T. Barlow and W. Smith, *J. Am. Acad. Orthop. Surg.*, 2015, **23**, 143–153.

4 D. S. Sparks, S. Saifzadeh, F. M. Savi, C. E. Dlaska, A. Berner, J. Henkel, J. C. Reichert, M. Wullschleger, J. Y. Ren, A. Cipitria, J. A. McGovern, R. Steck, M. Wagels, M. A. Woodruff, M. A. Schuetz and D. W. Hutmacher, *Nat. Protoc.*, 2020, **15**, 877–924.

5 J. A. Planell, *Bone repair materials*, CRC Press, Oxfordshire, UK, 2009.

6 G. L. Koons, M. Diba and A. G. Mikos, *Nat. Rev. Mater.*, 2020, **5**, 584–603.

7 K. L. Christman, *Science*, 2019, **363**, 340–341.

8 Y. J. Wang, *J. Mater. Sci. Technol.*, 2016, **32**, 801–809.

9 X. X. Xu, Z. J. Jia, Y. F. Zheng and Y. J. Wang, *Matter*, 2021, **4**, 2648–2650.

10 H. L. Zhu, S. Z. Zhu, Z. Jia, S. Parvinian, Y. Y. Li, O. Vaaland, L. B. Hu and T. Li, *Proc. Natl. Acad. Sci. U. S. A.*, 2015, **112**, 8971–8976.

11 N. Rauner, M. Meuris, M. Zoric and J. C. Tiller, *Nature*, 2017, **543**, 407–410.

12 L. B. Mao, H. L. Gao, H. B. Yao, L. Liu, H. Cölfen, G. Liu, S. M. Chen, S. K. Li, Y. X. Yan, Y. Y. Liu and S. H. Yu, *Science*, 2016, **354**, 107–110.

13 Q. F. Guan, Z. M. Han, H. B. Yang, Z. C. Ling and S. H. Yu, *Natl. Sci. Rev.*, 2021, **8**, nwaa230.

14 Z. M. Liu, C. Y. Shao, B. Jin, Z. S. Zhang, Y. Q. Zhao, X. R. Xu and R. K. Tang, *Nature*, 2019, **574**, 394–398.

15 Z. Mu, K. R. Kong, K. Jiang, H. L. Dong, X. R. Xu, Z. M. Liu and R. K. Tang, *Science*, 2021, **372**, 1466–1470.

16 J. Nowitzke and I. Popa, *J. Phys. Chem. Lett.*, 2022, **13**, 7139–7146.

17 M. Bonn and J. Hunger, *Science*, 2021, **371**, 123–124.

18 M. L. Lo Presti, G. Rizzo, G. M. Farinola and F. G. Omenetto, *Adv. Sci.*, 2021, **8**, e2004786.

19 Y. Yanagisawa, Y. L. Nan, K. Okuro and T. Aida, *Science*, 2018, **359**, 72–76.

20 P. Bertsch, M. Diba, D. J. Mooney and S. C. G. Leeuwenburgh, *Chem. Rev.*, 2023, **123**, 834–873.

21 B. Jiang, C. J. Chen, Z. Q. Liang, S. M. He, Y. D. Kuang, J. W. Song, R. Y. Mi, G. G. Chen, M. L. Jiao and L. B. Hu, *Adv. Funct. Mater.*, 2020, **30**, 1906307.

22 M. Z. Du, J. D. Chen, K. H. Liu, H. R. Xing and C. Song, *Composites, Part B*, 2021, **215**, 108790.

23 H. Peng, D. Zhang, B. Sun, Y. Luo, S. Lv, J. Wang and J. Chen, *RSC Adv.*, 2016, **6**, 12414–12421.

24 V. E. Bosio, C. Rybner and D. L. Kaplan, *J. Mater. Chem. B*, 2023, **11**, 7998–8006.

25 Y. Yang, Y. T. Lu, K. Zeng, T. Heinze, T. Groth and K. Zhang, *Adv. Mater.*, 2021, **33**, e2000717.

26 X. P. Yang, S. K. Biswas, J. Q. Han, S. Tanpichai, M. C. Li, C. C. Chen, S. L. Zhu, A. K. Das and H. Yano, *Adv. Mater.*, 2021, **33**, e2002264.

27 S. C. Camarero Espinosa, T. Kuhnt, E. J. Foster and C. Weder, *Biomacromolecules*, 2013, **14**, 1223–1230.

28 R. Sato, T. Arita, R. Shimada, T. Nohara, K. Tabata, K. Koseki, K. Umemoto and A. Masuhara, *Cellulose*, 2021, **28**, 871–879.

29 Q. Y. Liang, X. J. Gong, J. C. Liu, C. M. Ke, J. Dong, G. S. Song, P. Feng, H. K. Yu, X. F. Yang, J. Cui, C. L. Deng, Z. Y. Li, S. Liu and G. Z. Zhang, *Anal. Chem.*, 2023, **95**, 1318–1326.

30 C. Rey, J. L. Miquel, L. Facchini, A. P. Legrand and M. J. Glimcher, *Bone*, 1995, **16**, 583–586.

31 Y. C. Lin, J. M. Cho, G. A. Tompsett, P. R. Westmoreland and G. W. Huber, *J. Phys. Chem. C*, 2009, **113**, 20097–20107.

32 L. F. Zhang, H. Wang, R. Car and W. N. E, *Phys. Rev. Lett.*, 2021, **126**, 236001.

33 V. Kapil, C. Schran, A. Zen, J. Chen, C. J. Pickard and A. Michaelides, *Nature*, 2022, **609**, 512–516.

34 X. Y. Zheng, H. Lee, T. H. Weisgraber, M. Shusteff, J. DeOtte, E. B. Duoss, J. D. Kuntz, M. M. Biener, Q. Ge, J. A. Jackson, S. O. Kucheyev, N. X. Fang and C. M. Spadaccini, *Science*, 2014, **344**, 1373–1377.

35 H. Ping, W. Wagermaier, N. Horbelt, E. Scoppola, C. H. Li, P. Werner, Z. Y. Fu and P. Fratzl, *Science*, 2022, **376**, 188–192.

36 B. C. White, A. Garland and B. L. Boyce, *Matter*, 2023, **6**, 570–582.

37 B. H. Yu, C. C. Pletka and J. Iwahara, *J. Phys. Chem. B*, 2020, **124**, 1065–1070.

38 W. Zhao, J. Tropp, B. Qiao, M. Pink, J. D. Azoulay and A. H. Flood, *J. Am. Chem. Soc.*, 2020, **142**, 2579–2591.

39 G. X. Xu and X. Y. Wang, *Matter structure*, Science Press, Beijing, P. R. China, 2010.

40 H. Y. Liang, T. Q. Yin, M. Q. Liu, C. H. Fu, X. J. Xia, S. J. Zou, X. J. Hua, Y. H. Fu and Y. F. Bu, *J. Phys. Chem. Lett.*, 2023, **14**, 453–459.

41 D. Lee, C. Leroy, C. Crevant, L. Bonhomme-Coury, F. Babonneau, D. Laurencin, C. Bonhomme and G. D. De Paëpe, *Nat. Commun.*, 2017, **8**, 14104.

42 C. Y. Shao, H. L. Chang, M. Wang, F. Xu and J. Yang, *ACS Appl. Mater. Interfaces*, 2017, **9**, 28305–28318.

43 M. P. Rao, A. J. Sánchez-Herencia, G. E. Beltz, R. M. McMeeking and F. F. Lange, *Science*, 1999, **286**, 102–105.

44 M. Beaumont, P. Jusner, N. Gierlinger, A. W. T. King, A. Potthast, O. J. Rojas and T. Rosenau, *Nat. Commun.*, 2021, **12**, 2513.

45 R. Mao, N. Meng, W. Tu and T. Peijs, *Cellulose*, 2017, **24**, 4627–4639.

46 H. Peterlik, P. Roschger, K. Klaushofer and P. Fratzl, *Nat. Mater.*, 2006, **5**, 52–55.

47 J. E. Coleman, *Annu. Rev. Biophys. Biomol. Struct.*, 1992, **21**, 441–483.

48 S. Vimalraj, *Gene*, 2020, **754**, 144855.

49 A. Salhotra, H. N. Shah, B. Levi and M. T. Longaker, *Nat. Rev. Mol. Cell Biol.*, 2020, **21**, 696–711.

50 C. E. Jacome-Galarza, G. I. Percin, J. T. Muller, E. Mass, T. Lazarov, J. Eitler, M. Rauner, V. K. Yadav, L. Crozet, M. Bohm, P. L. Loyher, G. Karsenty, C. Waskow and F. Geissmann, *Nature*, 2019, **568**, 541–545.

51 X. Y. Li, Q. Zou, H. Chen and W. Li, *Sci. Adv.*, 2019, **5**, eaay6484.

52 J. C. Reichert, A. Cipitria, D. R. Epari, S. Saifzadeh, P. Krishnakanth, A. Berner, M. A. Woodruff, H. Schell, M. Mehta, M. A. Schuetz, G. N. Duda and D. W. Hutmacher, *Sci. Transl. Med.*, 2012, **4**, 141ra93.

53 G. G. Zhang, J. Kim, S. Hassan and Z. G. Suo, *Proc. Natl. Acad. Sci. U. S. A.*, 2022, **119**, e2203962119.

54 L. B. Mao, Y. F. Meng, X. S. Meng, B. Yang, Y. L. Yang, Y. J. Lu, Z. Y. Yang, L. M. Shang and S. H. Yu, *J. Am. Chem. Soc.*, 2022, **144**, 18175–18194.

55 H. W. Zhao, S. J. Liu, Y. Wei, Y. H. Yue, M. R. Gao, Y. B. Li, X. L. Zeng, X. L. Deng, N. A. Kotov, L. Guo and L. Jiang, *Science*, 2022, **375**, 551–556.